


# Temperature-Dependent Mechanism of Magnetization Reversal in the Spintronic Electrode Material $\text{La}_{0.67}\text{Sr}_{0.33}\text{MnO}_3$

W. Yan<sup>1,2,\*</sup>, L.C. Phillips,<sup>1</sup> and N.D. Mathur<sup>1,†</sup>

<sup>1</sup>*Department of Materials Science, University of Cambridge, Cambridge CB3 0FS, United Kingdom*

<sup>2</sup>*School of Physics & Astronomy, University of Nottingham, Nottingham NG7 2RD, United Kingdom*

 (Received 14 October 2019; revised 28 July 2022; accepted 5 October 2022; published 28 November 2022)

We investigate magnetization-reversal processes in half-metallic epitaxial films of  $\text{La}_{0.67}\text{Sr}_{0.33}\text{MnO}_3$  on  $\text{SrTiO}_3$  (110) substrates. At 150 K, major-loop magnetization reversal (MLMR) occurs beyond minor-loop switching fields, implying that MLMR is limited by domain nucleation. At 280 K, MLMR overlaps with minor-loop switching fields if there are deliberately introduced precipitates, implying that the precipitates limit MLMR by pinning domain walls. To confirm that the precipitates pin domain walls at 280 K, we use a two-dimensional analogue of the Gaunt pinning model to show that pinning-limited switching occurs at fields consistent with the observed precipitate density of  $0.3\text{--}2.0\ \mu\text{m}^{-2}$ . Our work demonstrates that comparing major and minor loops at any temperature of interest represents a simple way to check whether spintronic electrode materials show nucleation-limited MLMR, as circumstantially required for single-domain switching in micron-scale elements of  $\text{La}_{0.67}\text{Sr}_{0.33}\text{MnO}_3$  that represent spintronic electrodes [L. C. Phillips *et al.*, *Phys. Rev. Appl.* 4, 064004 (2015)].

DOI: [10.1103/PhysRevApplied.18.054084](https://doi.org/10.1103/PhysRevApplied.18.054084)

## I. INTRODUCTION

Spintronic devices exploit the spin of the electron to store and process information. They currently include commercial magnetic sensors [1] and magnetoresistive random-access memory [2] and may, in future, include devices that integrate memory and logic [3–5]. Good spintronic performance depends on the performance of the magnetic electrodes, the parallel and antiparallel magnetizations of which yield low and high states of two-terminal electrical resistance, respectively. The ferromagnetic perovskite  $\text{La}_{0.67}\text{Sr}_{0.33}\text{MnO}_3$  (LSMO) is a particularly attractive spintronic electrode because it is fully spin polarized at low temperature and has thus been used in magnetic tunnel junctions [6–12], molecular spintronic devices [13,14], and long-distance spin transport through carbon nanotubes [15] and graphene [16]. However, the large low-temperature magnetoresistance in these devices tends to deteriorate at higher temperatures, falling to zero well below the Curie temperature of  $T_C \sim 370$  K. This fall is traditionally associated with the suppression of  $T_C$  at interfaces and surfaces [17–19], but hitherto it has not been widely appreciated that this fall can also arise if magnetization reversal no longer proceeds by sharp switching at higher temperatures [20]. Here, we show that, for any given temperature below  $T_C$ , macroscopic magnetization data for

unpatterned films (with and without precipitates) can—and should—be used to identify magnetization-reversal processes to predict whether patterned elements will display the single-domain switching required of spintronic electrodes.

It is well known in the context of permanent magnets [21] that magnetic switching is affected by both magnetic anisotropy and microstructure. In small and microstructurally homogeneous samples, magnetization reversal occurs via coherent rotation and curling processes that are primarily parameterized by magnetic anisotropy alone. In large samples, magnetization reversal requires nucleation of domains at surfaces and defects, as well as depinning of domain walls (DWs) that then propagate, such that the coercive field,  $H_c$  is determined by the field required for nucleation or depinning, whichever is larger. In traditional hard magnets, such as Nd-Fe-B [22] and Sm-Co [23,24], the complex microstructures of which are designed to increase coercivity, the dominant magnetization-reversal mechanism is typically difficult to establish because it involves temperature-dependent transitions between nucleation-limited regimes and pinning-limited regimes [22–24]. Intriguingly, no such regimes have been identified in epitaxial thin films of the well-known spintronic electrode material LSMO [6–16].

Magnetization reversal that involves nucleation and/or pinning has previously been identified in films of LSMO (110) and LSMO (001) by measuring the angular dependence of major-loop coercivity [25,26] (we index LSMO

\*wenjing.yan@nottingham.ac.uk

†ndm12@cam.ac.uk

films as pseudocubic throughout this paper). However, nucleation-limited processes cannot be distinguished from pinning-limited processes, and the measurements are performed only at room temperature. Here, we use precipitate-containing epitaxial films of LSMO (110) to show that comparing major and minor easy-axis magnetic hysteresis loops [20,27] can distinguish nucleation-limited major-loop magnetization reversal (MLMR) at 150 K from pinning-limited MLMR at 280 K. Our findings reveal that precipitates confer complexity on epitaxial films, just as microstructure confers complexity on permanent magnets [22–24]. We choose LSMO (110) over LSMO (001) because it is known from magnetic imaging that sufficiently small ( $5 \times 5 \mu\text{m}^2$ ) elements of precipitate-free LSMO films at 150 K show nucleation-limited single-domain magnetization reversal if (110) oriented and pinning-limited gradual magnetization reversal if (001) oriented [16,20]. Therefore, LSMO (110) constitutes a suitable host in which to introduce temperature-dependent magnetization-reversal processes via precipitates, the role of which we confirm using a two-dimensional (2D) Gaunt pinning model that we derive from the three-dimensional (3D) Gaunt pinning model [28].

The thermally driven transition from nucleation-limited MLMR to pinning-limited MLMR represents a hitherto neglected reason for poor spintronic performance. More generally, magnetization-reversal processes identified at one temperature cannot be assumed to hold at other temperatures, such that magnetization-reversal processes should be tested at any given temperature of interest. Our work on continuous films of LSMO (110) shows that a comparison of major and minor easy-axis magnetic hysteresis loops represents a simple way of checking whether magnetization reversal is nucleation limited, as required to anticipate single-domain magnetic switching in patterned elements, such as spintronic electrodes.

## II. METHODS

### A. Experimental methods

Epitaxial films of LSMO (110) are grown on SrTiO<sub>3</sub> (STO) (110) by pulsed laser deposition, as described in Ref. [17]. Two equivalent films [Film A (65 nm) and Film B (69 nm), Figs. 1–3] are prepared, along with a third sample [Film C (34 nm), Fig. 4] that is precipitate-free because we use an aperture to crop the inhomogeneous periphery of the laser beam [29]. Film C is thinner because we do not increase the number of laser pulses after cropping the beam, as increasing the number of pulses would unduly compromise the LSMO target. However, the thinner film is equivalent to the thicker films both structurally and magnetically. Structural equivalence follows because even the thicker films are coherently strained (Fig. 1). Magnetic equivalence follows because even the thinner film is just thick enough to contain Bloch-like magnetic domain

walls, as verified using micromagnetic simulations that are similar to those we show later.

Atomic force microscopy (AFM) is performed using a Digital Instruments Nanoscope (III). Film thickness, crystal structure, and strain are studied using a PANalytical PW3050/65 X'Pert Pro high-resolution x-ray diffractometer. Magnetic measurements are made with a Princeton MicroMag 390 vibrating sample magnetometer (VSM). Prior to measuring minor loops, LSMO films are demagnetized either by heating to 150 °C in air or by applying an ac magnetic field, the magnitude of which is decreased by 1% per cycle.

### B. Micromagnetic simulations

We use the OOMMF micromagnetic package [30] for simulations that are similar to those detailed in our previous work [20], except here we model infinite strips of  $1 \mu\text{m}$  width with periodic boundary conditions that are implemented using the method described in Ref. [31]. The  $1 \mu\text{m}$  strip width is much larger than our 34–65 nm film thickness, such that the aspect ratio of our unpatterned LSMO (110) films is represented sufficiently well. We use a cubic mesh, the 4-nm cell of which is similar to the LSMO exchange length,  $\sqrt{2A/\mu_0 M_s^2} = 3.9 \text{ nm}$  ( $\mu_0$  is the permeability of free space). We use parameters (exchange constant,  $A$ ; saturation magnetization,  $M_s$ ; in-plane uniaxial magnetic anisotropy constant,  $K_{\text{IP}}$ ) for which values are listed in Table I for each temperature of interest (150 and 280 K), and we use out-of-plane anisotropy constant  $K_{\text{OOP}} = 5.5 K_{\text{IP}}$  (Appendix B).

## III. RESULTS AND DISCUSSION

### A. Structural data and magnetometry

First, we present structural and magnetic data for the two equivalent films that contain precipitates (Film A and Film B, Figs. 1–3). Then we present structural and magnetic data for the film that contains no precipitates (Film C, Fig. 4).

AFM measurements of surface topography [Fig. 1(a)] reveal a film roughness of 0.1 nm and precipitates of width  $W \sim 100 \text{ nm}$ , height  $\sim 4 \text{ nm}$ , and areal density  $\rho \sim 0.7 \mu\text{m}^{-2}$ . Six similar measurements of different areas show that  $\rho$  varies in the range 0.3–2.0  $\mu\text{m}^{-2}$ . An x-ray  $\omega$ - $2\theta$  scan that includes the 220 reflection of the STO substrate [Fig. 1(b)] is used to evaluate an out-of-plane LSMO lattice parameter of 5.455 Å. This lattice parameter is consistent with the value in Ref. [25], and it is smaller than the value of 5.465 Å for bulk LSMO because the epitaxial film is under coherent in-plane biaxial tensile strain [Figs. 1(c) and 1(d)].

Epitaxial LSMO (110) films on STO (110) substrates possess an in-plane easy axis along the in-plane  $\langle 100 \rangle$  direction, while the orthogonal in-plane and out-of-plane

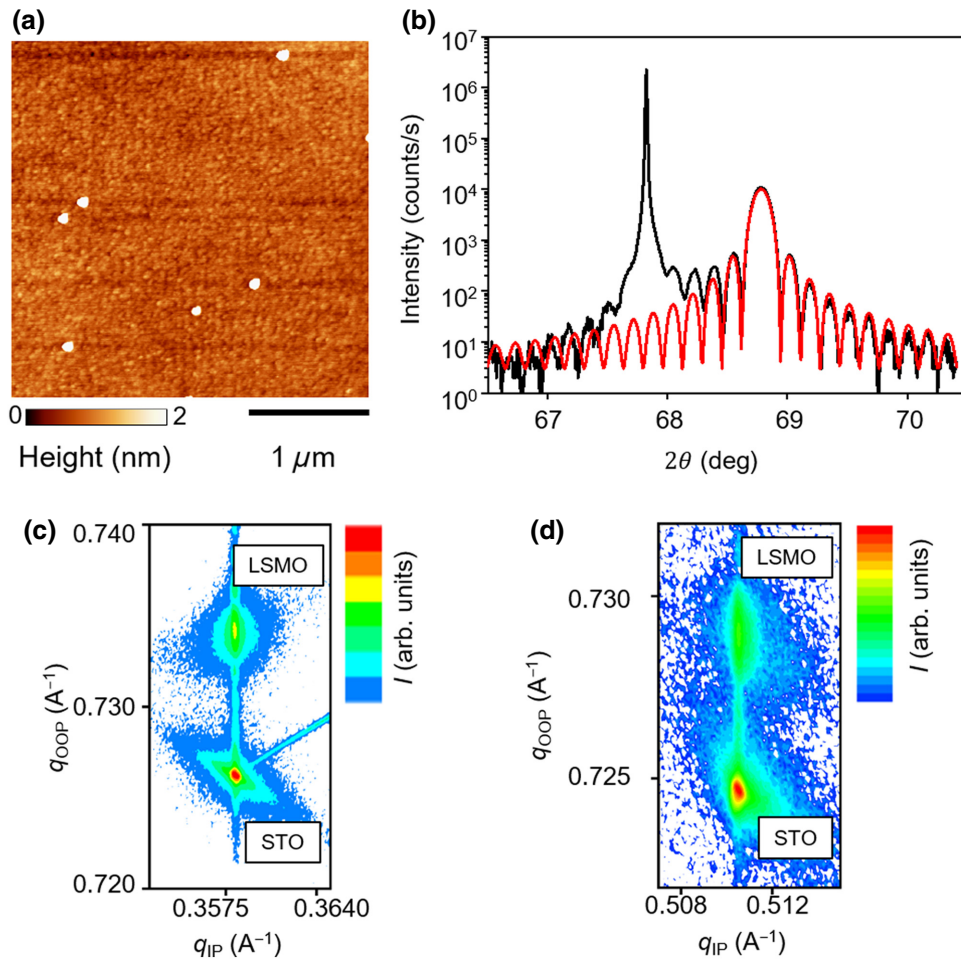


FIG. 1. LSMO film characterization. (a) AFM image. (b) X-ray diffraction  $\omega-2\theta$  scan of LSMO//STO (black), showing the 220 reflection from the STO substrate (tallest peak) and the corresponding reflection from the film (second-tallest peak, somewhat obscured by red fit data). Our fit (red) to film data gives a film thickness of  $t=65$  nm. X-ray reciprocal space maps around (c) 130 and (d) 222 reflections of LSMO confirm that the film is fully strained. Reciprocal lattice units  $q_{IP}$  and  $q_{OOP}$  correspond to inverse lattice spacings along the in-plane (IP) and out-of-plane (OOP) directions, respectively;  $I$  denotes x-ray intensity. Data in (a),(b) for Film A of thickness 65 nm; data in (c),(d) for Film B of thickness 69 nm.

$\langle 110 \rangle$  directions are hard [29]. Figure 2 presents a 280 K plot of the in-plane hard-axis magnetization,  $M$ , versus applied field,  $H$ . The constant that describes the in-plane

uniaxial magnetic anisotropy,  $K_{IP}(280 \text{ K}) = 4200 \text{ J m}^{-3}$ , is determined from data in Fig. 2 using the Stoner-Wohlfarth (SW) model [27]:

$$K_{IP} \frac{M}{M_s} = \mu_0 M_s H, \quad (1)$$

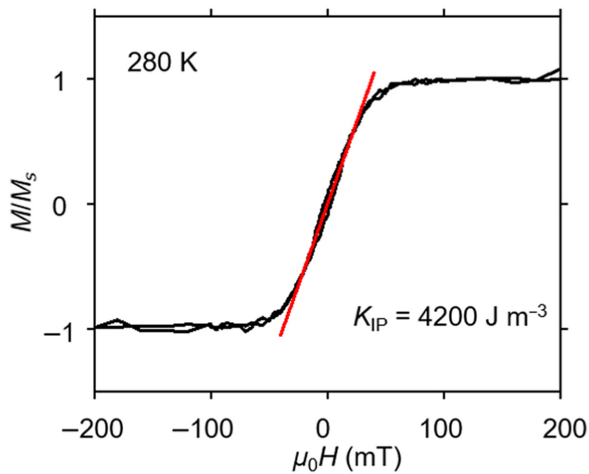


FIG. 2. In-plane hard-axis LSMO magnetization at 280 K. Magnetization,  $M$ , versus collinear field,  $H$ , with saturation magnetization  $M_s = 1.86 \mu_B \text{ Mn}^{-1}$ . Constant  $K_{IP}$  describing the in-plane uniaxial magnetic anisotropy is identified from the fit (red line) via Eq. (1). Data for Film B are measured along the collinear  $\langle 110 \rangle$  directions that lie in plane.

where  $M/H$  is determined via a linear fit (red) to data acquired during coherent rotation, and where the saturation magnetization is  $M_s(280 \text{ K}) = 1.86 \mu_B \text{ Mn}^{-1}$ . The corresponding values at 150 K are  $M_s(150 \text{ K}) = 3.23 \mu_B \text{ Mn}^{-1}$  and  $K_{IP}(150 \text{ K}) \sim 27800 \text{ J m}^{-3}$  (Appendix A).

Magnetization reversal at 150 and 280 K is studied at each temperature by comparing minor (black) and major (red) in-plane easy-axis hysteresis loops [Figs. 3(a) and 3(b)]. The minor loops are measured by increasing the amplitude of the field in each consecutive cycle after having first demagnetized the sample to create domains, such that minor-loop switching is limited by DW depinning at pinning fields of  $\pm H_p$ . At 150 K, MLMR occurs beyond the range of pinning fields  $\pm H_p$  identified from minor loops, and thus, the major-loop switching fields are deduced to be nucleation fields  $\pm H_n$  ( $|H_n| > |H_p|$ ) implies nucleation-limited MLMR). At 280 K, MLMR occurs at fields that are similar to the range of pinning fields  $\pm H_p$  identified from minor loops, and thus, the major-loop

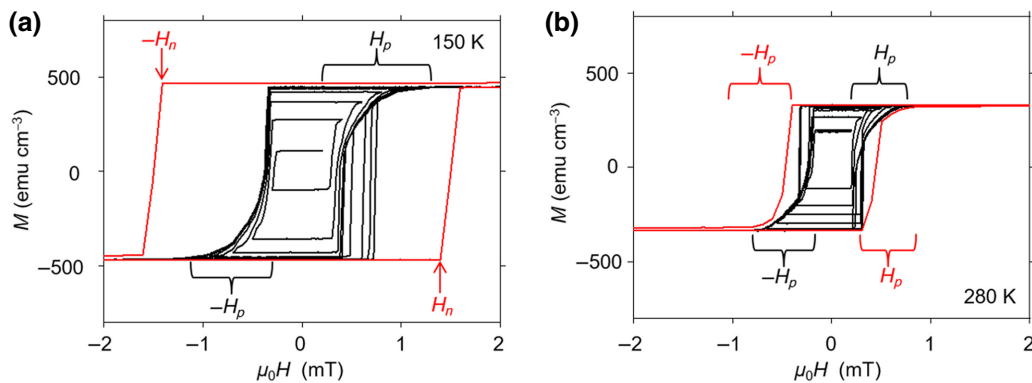


FIG. 3. Transition from pinning-limited MLMR to nucleation-limited MLMR in LSMO (110). At (a) 150 K and (b) 280 K, we show in-plane easy-axis measurements of magnetization,  $M$ , versus field,  $H$ . Major loops (red) are accompanied by minor loops (black) for which the film is demagnetized prior to increasing field amplitude in each consecutive cycle. In (a),  $\mu_0|H_n| \sim 1.4$  mT (major loop) is less than  $\mu_0|H_p| \sim 0.24$ – $1.28$  mT (minor loops), so MLMR (red) is nucleation limited. In (b),  $\mu_0|H_p| \sim 0.17$ – $0.71$  mT (minor loops) has some overlap with  $\mu_0|H_n| \sim 0.32$ – $0.8$  mT (major loop), so MLMR (red) is pinning limited. Data for Film A are measured up to 100 mT along the collinear  $\langle 100 \rangle$  directions that lie in plane.

switching fields are deduced to be pinning fields  $\pm H_p$  that lie beyond unobserved nucleation fields  $\pm H_n$  ( $|H_n| < |H_p|$  implies pinning-limited MLMR). Increasing the temperature from 150 to 280 K thus induces a transition from nucleation-limited MLMR to pinning-limited MLMR.

Let us now consider room-temperature magnetization reversal in our film with no precipitates [Fig. 4(a)] by comparing minor (black) and major (red) in-plane easy-axis hysteresis loops [Fig. 4(b)]. MLMR [red data, Fig. 4(b)] occurs at fields that lie almost wholly beyond the range of pinning fields  $\pm H_p$  identified from minor loops [black

data, Fig. 4(b)], and thus, the major-loop switching fields are deduced to be nucleation fields  $\pm H_n$ , such that MLMR in the precipitate-free film remains nucleation limited near room temperature. However, MLMR is not perfectly sharp because  $|H_n|$  lies close to  $|H_p|$ .

## B. Micromagnetic simulation

The micromagnetic OOMMF package is used to investigate DWs in 64-nm-thick LSMO films at both 150 and 280 K (Fig. 5). The DWs at both temperatures are stable,

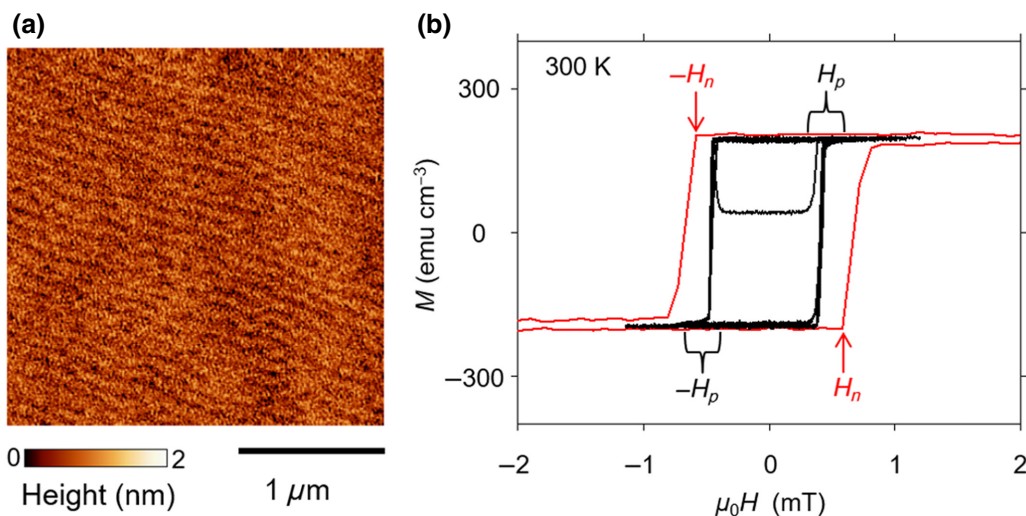


FIG. 4. Nucleation-limited MLMR in precipitate-free LSMO near room temperature. (a) AFM image showing step-terrace growth with no precipitates. (b) In-plane easy-axis measurements of magnetization,  $M$ , versus field,  $H$ , at 300 K. Major loop (red) is accompanied by minor loops (black) for which the film is demagnetized prior to increasing the field amplitude in each consecutive cycle. Switching in the range  $\mu_0|H_p| \sim 0.28$ – $0.72$  mT (minor loop) is almost complete by  $\mu_0|H| \sim 0.48$  mT, which lies below  $\mu_0|H_n| \sim 0.58$  mT (major loop), such that MLMR (red) is nucleation limited. Magnetic data are measured up to 300 mT along the collinear  $\langle 100 \rangle$  directions that lie in plane. All data for Film C.



TABLE I. DW width and expected pinning field. For both 150 and 280 K, domain-wall width,  $W_d$ , and expected pinning field,  $H_{EP}$ , are derived from data in the other columns via micromagnetic simulation and the 2D Gaunt pinning model, respectively. Variations of precipitate width,  $W$ , may be ignored, as  $W_d \ll W$  (Appendix C2).

$T$ (K)	$M_s$ (A m $^{-1}$ )	$K_{IP}$ (J m $^{-3}$ )	$A$ (J m $^{-1}$ )	$\gamma$ (J m $^{-1}$ )	$\rho$ ( $\mu\text{m}^{-2}$ )	$t$ (nm)	$W$ (nm)	$W_d$ (nm)	$\mu_0 H_{EP} $ (mT)
150	$4.67 \times 10^5$	$2.78 \times 10^4$	$2.1 \times 10^{-12}$	$1.03 \times 10^{-10}$	0.3–2.0	65	100	4	0.88–2.27
280	$3.33 \times 10^5$	$4.2 \times 10^3$	$1.2 \times 10^{-12}$	$4.0 \times 10^{-11}$				6	0.48–1.23

Bloch-like, slightly asymmetric, and with little stray field, as expected for LSMO (110) [20], and more generally with similar input parameters [32]. The increase of total energy (stray-field energy, demagnetizing-field energy, exchange energy, and anisotropy energy) due to the presence of a DW is  $\gamma = 103 \text{ pJ m}^{-1}$  (150 K) and  $40 \text{ pJ m}^{-1}$  (280 K) per unit length of DW. We find DW widths of  $W_d = 2\sigma = 4 \text{ nm}$  (150 K) and  $6 \text{ nm}$  (280 K), where  $\sigma$  is the Gaussian standard deviation obtained from one-dimensional (1D) plots of DW energy versus in-plane distance from the DW (these 1D plots of energy are obtained by averaging energy-density maps [Figs. 5(d) and 5(h)] along the out-of-plane direction). The simulated DW widths are much narrower than our precipitates of width  $W \sim 100 \text{ nm}$  [Fig. 1(b)], implying that each precipitate wholly eliminates a DW segment of length  $W$ , thus saving energy  $\gamma W$ . (It is possible that precipitates do not fully eliminate DWs [33], such that

the energy saved is reduced by a small factor of  $\alpha \sim 0.5$ –1 to  $\alpha\gamma W$ , but we will assume  $\alpha = 1$ .)

### C. 2D analogue of the Gaunt pinning model

The Gaunt pinning model [28] is used to derive a 2D Gaunt pinning model (Appendix C) from which we predict the DW pinning field,  $H_{EP}$  (Table I) due to an attractive pinning force,  $f$ , from precipitates:

$$H_{EP} = \frac{1}{\mu_0 M_s t} \left( \frac{f}{2} \right)^{3/2} \left( \frac{\rho}{\gamma} \right)^{1/2}, \quad (2)$$

$$f = \frac{2\alpha\gamma W}{(W^2 + W_d^2)^{1/2}} \exp\left(-\frac{1}{2}\right). \quad (3)$$

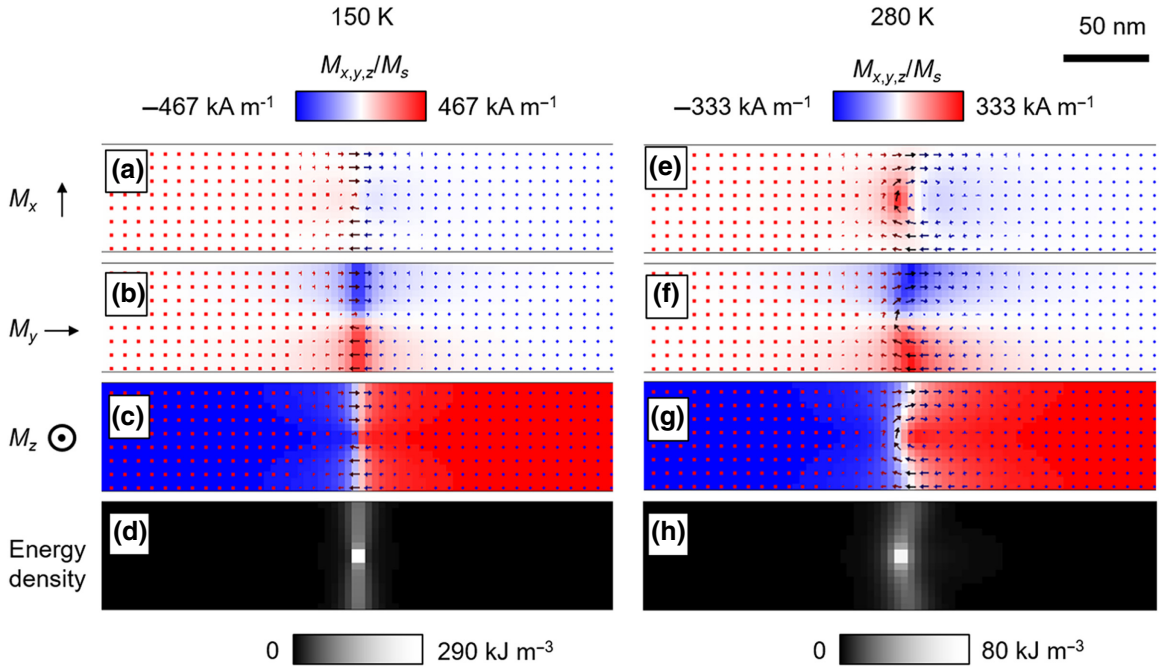


FIG. 5. Simulations of magnetization and energy for a DW in 64-nm-thick LSMO (011) films. For (a)–(d) 150 K and (e)–(h) 280 K, all panels present the same  $x$ - $y$  cross section of the film containing a DW, and there is  $z$ -axis translational symmetry. Color shading and arrows present the same information. Color shading shows (a),(e)  $M_x/M_s$  along the out-of-plane hard axis (collinear  $\langle 110 \rangle$  directions), (b),(f)  $M_y/M_s$  along the in-plane hard axis (collinear  $\langle 110 \rangle$  directions), and (c),(g)  $M_z/M_s$  along the in-plane easy axis (collinear  $\langle 100 \rangle$  directions). Arrows show the local magnetization direction and are colored red ( $M_z/M_s > 0$ ), blue ( $M_z/M_s < 0$ ), and brown ( $M_z/M_s \sim 0$ ).  $M_s(150 \text{ K}) = 467 \text{ kA m}^{-1}$ ,  $M_s(280 \text{ K}) = 333 \text{ kA m}^{-1}$ . (d),(h) Corresponding energy-density maps. Volume-normalized units are consistent with  $z$ -axis translational symmetry.

As a reminder,  $M_s$  is saturation magnetization,  $t$  is film thickness,  $\rho$  is areal precipitate density,  $\gamma$  is DW energy per unit length of DW, DW energy saving is reduced from  $\gamma W$  to  $\alpha\gamma W$  if precipitates do not wholly eliminate DWs [33] but here we assume  $\alpha = 1$ ,  $W$  is precipitate width, and  $W_d$  is DW width. In practice, our model predicts a range of pinning field values,  $H_{EP}$ , because the areal precipitate density,  $\rho$ , is presented as a range to reflect the observed variation.

At 150 K, our model predicts values of  $\mu_0|H_{EP}| = 0.88\text{--}2.27$  mT, which are similar to the measured values of  $\mu_0|H_p| = 0.24\text{--}1.28$  mT [minor loops, Fig. 3(a)]. At 280 K, our model predicts values of  $\mu_0|H_{EP}| = 0.44\text{--}1.13$  mT, which are similar to the measured values of  $\mu_0|H_p| = 0.31\text{--}0.90$  mT [major loops, Fig. 3(b)] and  $\mu_0|H_p| = 0.17\text{--}0.80$  mT [minor loops, Fig. 3(b)].

The transition from nucleation-limited MLMR to pinning-limited MLMR with increasing temperature can be understood via the following equations for nucleation and pinning fields (Appendix D):

$$H_p \propto M_s^{1.5}, \quad (4)$$

$$H_n \propto bM_s^{2.3} - N_{d,\text{eff}}M_s, \quad (5)$$

where  $b$  is a constant and  $N_{d,\text{eff}}$  is the local demagnetizing factor at the most favorable nucleation site. Upon increasing the temperature, the fall in  $M_s$  would cause  $H_n$  to fall faster than  $H_p$ , even without assistance from the  $-N_{d,\text{eff}}M_s$  term, such that  $H_p$  is liable to eventually exceed  $H_n$ .

#### IV. CONCLUSIONS

For epitaxial films of LSMO (110) with precipitates in an otherwise microstructurally simple matrix, we show that increasing the temperature from 150 to 280 K results in a transition from nucleation-limited MLMR to pinning-limited MLMR, consistent with a quantitative analysis in which we employ a 2D Gaunt pinning model that we derive from the 3D Gaunt pinning model [28]. For epitaxial films of LSMO (110) with no precipitates, we show that there is no such transition, thus confirming that the precipitates are responsible for the thermally driven change of MLMR mechanism. However, an absence of precipitates does not necessarily preclude pinning-limited magnetization reversal, as step edges and crystallographic defects can also pin DWs [34,35].

Given that the formation of magnetic domains during magnetization reversal severely compromises the performance of spintronic electrode materials [20], the pinning-limited MLMR that is responsible represents an important but hitherto neglected reason for the deterioration of spintronic device performance. Our simple method of studying magnetization reversal, which involves comparing major-loop and minor-loop switching fields [20,27], should be

widely employed to confirm that major-loop switching fields lie beyond minor-loop switching fields at any temperature of interest. This would confirm that magnetization reversal is nucleation limited, and thus, liable to proceed via single-domain switching in spintronic electrodes [20].

#### ACKNOWLEDGMENTS

We thank S. Chanattukuzhiyil and L. Fallarino for measuring some of the VSM data. This work is funded by a Schlumberger Cambridge International Scholarship and a University of Nottingham Anne McLaren Research Fellowship (W.Y.); and a UK EPSRC DTA grant and grant No. F/09 154/E from the Leverhulme Trust (L. C. P.).

#### DATA AVAILABILITY

All data are presented in the manuscript, and are available from the corresponding authors upon request.

#### APPENDIX A: LSMO AT 150 K

Changes of magnetic anisotropy due to changes of temperature (150 K  $\leftrightarrow$  280 K) arise primarily due to changes of saturation magnetization,  $M_s$ , via [36–38]

$$\frac{K_{IP}(280\text{ K})}{K_{IP}(150\text{ K})} = \left( \frac{M_s(280\text{ K})}{M_s(150\text{ K})} \right)^n. \quad (A1)$$

Using Film C, we establish  $n = 3.3$  for the strained material (LSMO) by measuring  $M_s(150\text{ K}) = 3.05 \mu_B \text{ Mn}^{-1}$  [Fig. 6(a)] and  $M_s(280\text{ K}) = 1.70 \mu_B \text{ Mn}^{-1}$  [Fig. 6(b)], and by using the SW model [Eq. (1)] with these values and the fits shown to identify  $K_{IP}(150\text{ K}) = 43\,000 \text{ J m}^{-3}$  and  $K_{IP}(280\text{ K}) = 6500 \text{ J m}^{-3}$ .

For Film B, we then identify  $K_{IP}(150\text{ K}) \sim 27\,800 \text{ J m}^{-3}$  from Eq. (A1) using  $n = 3.3$ , both  $M_s(280\text{ K}) = 1.86 \mu_B \text{ Mn}^{-1}$  and  $K_{IP}(280\text{ K}) = 4200 \text{ J m}^{-3}$  from the main text, and  $M_s(150\text{ K}) = 3.23 \mu_B \text{ Mn}^{-1}$  (Fig. 7).

#### APPENDIX B: OUT-OF-PLANE ANISOTROPY CONSTANT $K_{OOP}$

We use data for Film C at 300 K (Fig. 8) to determine the out-of-plane anisotropy constant,  $K_{OOP}$ , in terms of the in-plane uniaxial magnetic anisotropy constant,  $K_{IP}$ , and we assume this ratio to hold for all temperatures of interest.

We find  $K_{IP} = 6500 \text{ J m}^{-3}$  from Eq. (1) given that a saturation magnetization of  $M_s = 225 \text{ emu cm}^{-3} = 1.32 \mu_B \text{ Mn}^{-1} = 2.25 \times 10^5 \text{ A m}^{-1}$  is reached at a field of  $0.47 \times 10^5 \text{ A m}^{-1}$  (corresponding to 0.06 T) (red data, Fig. 8).

We find  $K_{OOP} = 1/2 \mu_0 M_s (H_{\text{sat},OOP} - M_s) = 35700 \text{ J m}^{-3}$ , given also that the field for saturation is

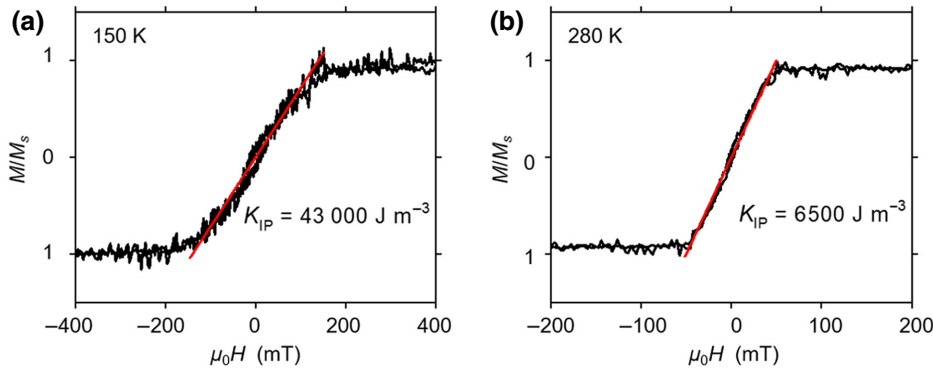


FIG. 6. In-plane hard-axis LSMO magnetization at different temperatures. Magnetization,  $M$ , versus field,  $H$ , at (a) 150 K and (b) 280 K. In each panel, the red-line fit is used to identify the anisotropy constant,  $K_{IP}$ , via Eq. (1). Data for Film C are measured along the collinear  $\langle 110 \rangle$  directions that lie in plane.

$4.77 \times 10^5 \text{ A m}^{-1}$  (corresponding to 0.6 T) (black data, Fig. 8).

Therefore,  $K_{OOP}/K_{IP} = 5.5$ , which we assume in our OOMMF simulations for both 150 and 280 K.

### APPENDIX C: DERIVATION OF THE GAUNT PINNING MODEL

#### 1. Expression for the pinning field

The following represents a 2D version of the 3D derivation in Ref. [28].

Figure 9 shows a  $180^\circ$  thin-film DW that is pinned between obstacles separated by distance  $2L_1$ . In magnetic field  $H$ , the DW bows out to perpendicular distance  $h_1$ , such that it forms an arc of radius  $R$ .

If  $R$  is much greater than both  $L_1$  and  $h_1$ , then we may approximately describe the arc as a parabola,  $y = f(x) =$

$-ax^2 + h_1$ , such that

$$f(L_1) = 0 \text{ and} \quad (\text{C1})$$

$$|\ddot{y}| = \frac{1}{R}, \quad (\text{C2})$$

where Eq. (C2) equates the second derivative of  $y$  to arc curvature  $1/R$ . From Eqs. (C1) and (C2), we find

$$y = -\frac{1}{2R}x^2 + h_1, \quad (\text{C3})$$

and

$$h_1 \approx \frac{L_1^2}{2R}. \quad (\text{C4})$$

The area enclosed between the DW and a straight line between the obstacles is found by integrating Eq. (C3)

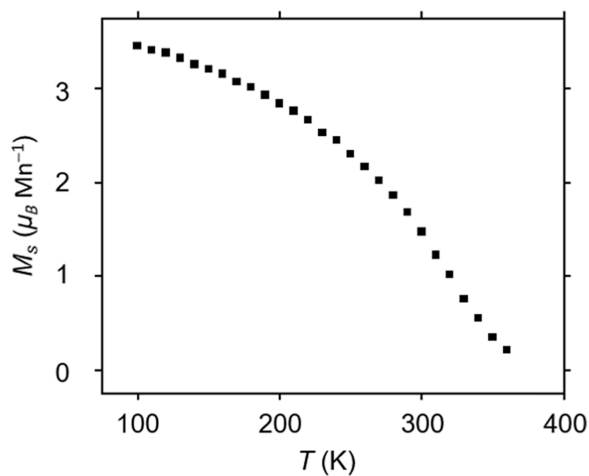


FIG. 7. LSMO saturation magnetization versus temperature. Values of saturation magnetization,  $M_s$ , are obtained from in-plane easy-axis  $M(H)$  measurements. Data for Film B are measured along the collinear  $\langle 100 \rangle$  directions that lie in plane.

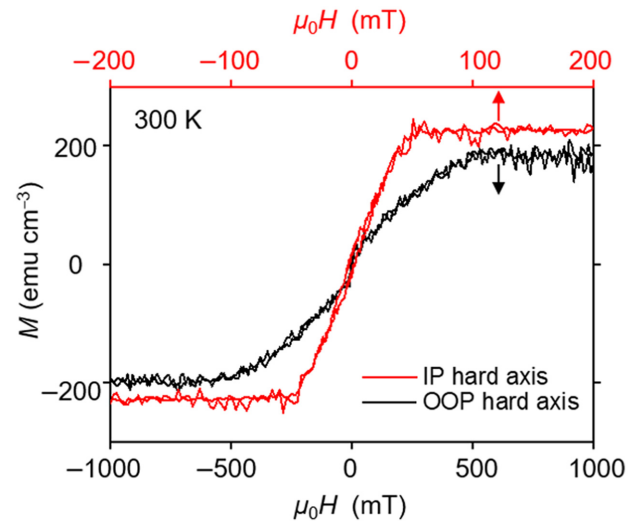


FIG. 8. In-plane and out-of-plane magnetic anisotropy at room temperature. Red (black) data show the in-plane (out-of-plane) hard-axis magnetization,  $M$ , as a function of field,  $H$ , at 300 K. Data for Film C are measured along the collinear  $\langle 110 \rangle$  directions that lie in plane (red) and the collinear  $\langle 110 \rangle$  directions that lie out of plane (black).

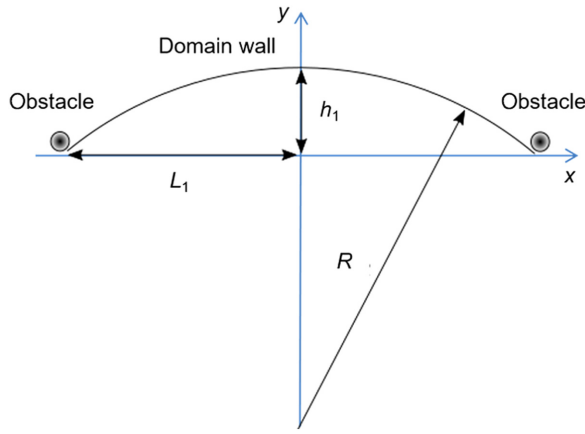


FIG. 9. DW bowing in a magnetic field. The DW is pinned by two obstacles separated by  $2L_1$ . It forms an arc, the vertex of which lies at  $(0, h_1)$ .

between  $-L_1$  and  $+L_1$ , and using Eq. (C4) to yield

$$A_1 = \int_{-L_1}^{L_1} \left( -\frac{1}{2R}x^2 + h_1 \right) dx \approx 2h_1L_1 - \frac{L_1^3}{3R} = \frac{2L_1^3}{3R}. \quad (\text{C5})$$

Let us now consider two similar and adjacent DWs that are pinned by three collinear precipitates (each pair is separated by  $2L_1$ ). If the DW breaks free from the central precipitate, then the situation in Fig. 9 is recovered with  $L_2 = 2L_1$ . The new area swept out by this event is

$$\Delta A = A_2 - 2A_1 = \frac{4L_1^3}{R}. \quad (\text{C6})$$

In the strong-pinning regime and under the Friedel steady-state criterion, we have  $\rho \Delta A = 1$ . This steady-state criterion states that the DW sweeps a volume containing, on average, one more precipitate during breakaway, where  $\rho$  is the areal density of pinning centers [28].

In a 2D thin film of thickness  $t$ , and during the breakaway event, the gain in DW energy equals exactly the loss in magnetic energy, which is represented by the Laplace formula. The DW of line energy  $\gamma$  in  $\text{J m}^{-1}$  is

$$\frac{\gamma}{Rt} = 2\mu_0 M_s H. \quad (\text{C7})$$

Using Eqs. (C6) and (C7), we can express the steady-state criterion as

$$8L_1^3 \mu_0 M_s H \rho t = \gamma. \quad (\text{C8})$$

Therefore, the value of the interobstacle distance,  $D = 2L_1$ , for the steady state is

$$D = (\gamma / \mu_0 M_s H \rho t)^{1/3}. \quad (\text{C9})$$

The expected coercive field when pinning is the limiting step is  $H_{\text{EP}} = f / 2\mu_0 M_s D t$  [Eq. (1) in Ref. [28]], assuming

a single obstacle interacting with the DW. Its value can be derived if the maximum pinning force,  $f$ , of the pinning center is known:

$$H_{\text{EP}} = \frac{1}{\mu_0 M_s t} \left( \frac{f}{2} \right)^{3/2} \left( \frac{\rho}{\gamma} \right)^{1/2}. \quad (\text{C10})$$

## 2. Estimate of the maximum pinning force

In Eq. (C10), the maximum pinning force,  $f$ , is the maximum gradient in a plot of energy versus distance when a DW travels through and interacts with a precipitate. The form of this relationship is generally nontrivial, and assuming these precipitates are nonmagnetic through-thickness particles, as in Ref. [33], we may assume that the particle interrupts the DW, causing an attractive interaction due to reduced DW length. The peak interaction energy, therefore, equals the energy associated with the missing DW, which is  $\gamma W$ , where  $W$  is the precipitate width. In the case where the precipitates are not through-thickness particles and cut through the domain wall partially, an additional factor,  $\alpha$ , is required to describe the interaction energy,  $e_0 = \alpha \gamma W$ .

We further assume that the energy-distance relationship is a Gaussian in this form:

$$E(x) = e_0 e^{(-x^2/2\sigma^2)}, \quad (\text{C11})$$

where the standard deviation,  $\sigma = 1/2(W^2 + W_d^2)^{1/2}$ , reflects the convolution of the particle width,  $W$ , with the domain width,  $W_d$ . The maximum force,  $f = (dE/dx)_{\text{max}}$ , occurs at the inflection point,  $x = \pm\sigma$ , of the Gaussian curve, such that

$$f = \frac{e_0}{\sigma} \exp\left(-\frac{1}{2}\right) = \frac{2\alpha\gamma W}{(W^2 + W_d^2)^{1/2}} \exp\left(-\frac{1}{2}\right). \quad (\text{C12})$$

In the limit  $W_d \ll W$ ,  $f = 2\gamma \exp(-1/2)$ , i.e.,  $f$  (and hence,  $H_{\text{EP}}$ ) are independent of  $W$ .

Combining Eqs. (C10) and (C12), we can quantitatively calculate the expected pinning field as a result of precipitates, as presented in Sec. III C.

## APPENDIX D: QUALITATIVE INTERPRETATION OF THE NUCLEATION AND PINNING FIELDS

Qualitatively, we can understand the transition from nucleation to pinning-limited reversal processes using the scaling relationships developed in Refs. [28,39]. This is derived for a 3D material, as the scaling laws are better established. The pinning field,  $H_p$ , and nucleation field,  $H_n$ ,



are expressed as

$$H_p \propto \rho_V f^2 / \gamma_V M_s, \quad (\text{D1})$$

$$H_n \sim \frac{2K_{\text{eff}}}{\mu_0 M_s} - N_{d,\text{eff}} M_s, \quad (\text{D2})$$

where  $f$  is the maximum restoring force of the pinning center,  $\rho_V$  is the pinning-center density per unit volume  $V$ ,  $\gamma_V$  is the DW energy per unit area, and the effective anisotropy  $K_{\text{eff}}$  and demagnetizing factor  $N_{d,\text{eff}}$  are difficult-to-estimate local parameters that describe the most-favorable nucleation site.

Using  $\gamma_V = \pi \sqrt{AK}$ , where  $A$  is the exchange stiffness and  $A \propto M^{5/3}$  [40], together with  $f \propto \gamma_V$  [28] and  $K_{\text{eff}} \propto M_s^a$  ( $a = 3.3$ , Appendix A), Eqs. (D1) and (D2) can be reduced to

$$H_p \propto M_s^{((a/2)-(1/6))} = M_s^{1.5}, \quad (\text{D3})$$

$$H_n \propto (bM_s^{a-1} - N_{d,\text{eff}} M_s) = (bM_s^{2.3} - N_{d,\text{eff}} M_s), \quad (\text{D4})$$

where  $b$  is a constant and  $N_{d,\text{eff}}$  is the demagnetizing factor.

- 
- [1] B. Filippitsch and M. Ortner, Magnetic field distortion from conductive layers for high-frequency speed sensor applications, *IEEE Trans. Magn.* **53**, 4003604 (2017).
- [2] C. Chappert, A. Fert, and F. Nguyen Van Dau, The emergence of spin electronics in data storage, *Nat. Mater.* **6**, 813 (2007).
- [3] I. Žutić, J. Fabian, and S. Das Sarma, Spintronics: Fundamentals and applications, *Rev. Mod. Phys.* **76**, 323 (2004).
- [4] H. Dery, P. Dalal, Ł Cywiński, and L. J. Sham, Spin-based logic in semiconductors for reconfigurable large-scale circuits, *Nature* **447**, 573 (2007).
- [5] B. Behin-Aein, D. Datta, S. Salahuddin, and S. Datta. Proposal for an all-spin logic device with built-in memory, *Nat. Nano* **5**, 266 (2010).
- [6] M. Bowen, M. Bibes, A. Barthélémy, J-P Contour, A. Anane, Y. Lemaître, and A. Fert, Nearly total spin polarization in  $\text{La}_{2/3}\text{Sr}_{1/3}\text{MnO}_3$  from tunnelling experiments, *Appl. Phys. Lett.* **82**, 233 (2003).
- [7] J. Z. Sun, W. J. Gallagher, P. R. Duncombe, L. Krusin-Elbaum, R. A. Altman, A. Gupta, Y. Lu, G. Q. Gong, and G. Xiao, Observation of large low-field magnetoresistance in trilayer perpendicular transport devices made using doped manganate perovskites, *Appl. Phys. Lett.* **69**, 3266 (1996).
- [8] Y. Lu, X. W. Li, G. W. Gong, G. Xiao, A. Gupta, P. Lecoeur, J. Z. Sun, Y. Y. Wang, and C. P. Dravid, Large magnetotunneling effect at low magnetic fields in micrometer-scale epitaxial  $\text{La}_{0.67}\text{Sr}_{0.33}\text{MnO}_3$  tunnel junctions, *Phys. Rev. B* **54**, R8357 (1996).
- [9] C. Kwon, Q. X. Jia, Y. Fan, M. F. Hundley, D. W. Reagor, J. Y. Coulter, and D. E. Peterson, Large magnetoresistance in  $\text{La}_{0.7}\text{Sr}_{0.3}\text{MnO}_3/\text{SrTiO}_3/\text{La}_{0.7}\text{Sr}_{0.3}\text{MnO}_3$  ramp-edge junctions, *Appl. Phys. Lett.* **72**, 486 (1998).
- [10] M. Bowen, A. Barthélémy, M. Bibes, E. Jacquet, J.-P. Contour, A. Fert, F. Ciccacci, L. Duo, and R. Bertacco, Spin-Polarized Tunneling Spectroscopy in Tunnel Junctions with Half-Metallic Electrodes, *Phys. Rev. Lett.* **95**, 137203 (2005).
- [11] V. Garcia, M. Bibes, L. Bocher, S. Valencia, F. Kronast, A. Crassous, X. Moya, S. Enouz-Vedrenne, A. Gloter, D. Imhoff, *et al.*, Ferroelectric control of spin polarisation, *Science* **327**, 1106 (2010).
- [12] Y. W. Yin, J. D. Burton, Y.-M. Kim, A. Y. Borisevich, S. J. Pennycook, S. M. Yang, T. W. Noh, A. Gruverman, X. G. Li, E. Y. Tsymbal, and Q. Li, Enhanced tunnelling electroresistance effect due to a ferroelectrically induced phase transition at a magnetic complex oxide interface, *Nat. Mater.* **12**, 397 (2013).
- [13] Z. H. Xiong, D. Wu, Z. Vally Vardeny, and Jing Shi, Giant magnetoresistance in organic spin-valves, *Nature* **427**, 821 (2004).
- [14] D. Sun, M. Feng, X. Xu, L. Jiang, H. Guo, Y. Wang, W. Yang, L. Yin, P. C. Snijders, T. Z. Ward, *et al.*, Active control of magnetoresistance of organic spin valves using ferroelectricity, *Nat. Commun.* **5**, 4396 (2014).
- [15] L. E. Hueso, J. M. Pruneda, V. Ferrari, G. Burnell, J. P. Valdés-Herrera, B. D. Simons, P. B. Littlewood, E. Artacho, A. Fert, and N. D. Mathur, Transformation of spin information into large electrical signals using carbon nanotubes, *Nature* **445**, 410 (2007).
- [16] W. Yan, L. C. Phillips, M. Barbone, S. J. Hämäläinen, A. Lombardo, M. Ghidini, X. Moya, F. Maccherozzi, S. van Dijken, S. S. Dhesi, *et al.*, Long Spin Diffusion Length in Few-Layer Graphene Flakes, *Phys. Rev. Lett.* **117**, 147201 (2016).
- [17] L. C. Phillips, F. Maccherozzi, X. Moya, M. Ghidini, W. Yan, J. Soussi, S. S. Dhesi, and N. D. Mathur, Tuning  $\text{La}_{0.67}\text{Sr}_{0.33}\text{MnO}_3$  surface magnetism using  $\text{LaMnO}_3$  and  $\text{SrTiO}_3$  caps, *J. Magn. Magn. Mater.* **355**, 331 (2014).
- [18] J.-H. Park, E. Vescovo, H.-J. Kim, C. Kwon, R. Ramesh, and T. Venkatesan, Magnetic Properties at Surface Boundary of a Half-Metallic Ferromagnet  $\text{La}_{0.7}\text{Sr}_{0.3}\text{MnO}_3$ , *Phys. Rev. Lett.* **81**, 1953 (1998).
- [19] V. Garcia, M. Bibes, A. Barthélémy, M. Bowen, E. Jacquet, J.-P. Contour, and A. Fert, Temperature dependence of the interfacial spin polarisation of  $\text{La}_{2/3}\text{Sr}_{1/3}\text{MnO}_3$ , *Phys. Rev. B* **69**, 052403 (2004).
- [20] L. Phillips, W. Yan, X. Moya, M. Ghidini, F. Maccherozzi, S. S. Dhesi, and N. D. Mathur, Control of Magnetization-Reversal Mechanism via Uniaxial Anisotropy Strength in  $\text{La}_{0.67}\text{Sr}_{0.33}\text{MnO}_3$  Electrodes for spintronic Devices, *Phys. Rev. Appl.* **4**, 064004 (2015).
- [21] J. D. Livingston, A review of coercivity mechanism, *J. Appl. Phys.* **52**, 2544 (1981).
- [22] K.-D. Durst and H. Kronmüller, The coercive field of sintered and melt-spun NdFeB magnets, *J. Magn. Magn. Mater.* **68**, 63 (1987).
- [23] D. Goll, H. Kronmüller, and H. H. Stadelmaier, Micromagnetism and the microstructure of high-temperature permanent magnets, *J. Appl. Phys.* **96**, 6534 (2004).
- [24] C. Rong, H. Zhang, B. Shen, and J. Ping Liu, Mechanism of the anomalous temperature dependence of coercivity in  $\text{Sm}(\text{Co}, \text{Fe}, \text{Cu}, \text{Zr})_z$  high-temperature magnets, *Appl. Phys. Lett.* **88**, 042504 (2006).

- [25] H. Boschker, J. Kautz, E. P. Houwman, G. Koster, D. H. A. Blank, and G. Rijnders. Magnetic anisotropy and magnetization reversal of  $\text{La}_{0.67}\text{Sr}_{0.33}\text{MnO}_3$  thin films on  $\text{SrTiO}_3$  (110), *J. Appl. Phys.* **108**, 103906 (2010).
- [26] M. Mathews, E. P. Houwman, H. Boschker, G. Rijnders, and D. H. A. Blank, Magnetization reversal mechanism in  $\text{La}_{0.67}\text{Sr}_{0.33}\text{MnO}_3$ , *J. Appl. Phys.* **107**, 013904 (2010).
- [27] B. D. Cullity and C. F. Graham, *Introduction to Magnetic Materials*, 2nd ed. (Wiley, Hoboken, NJ, USA, 2008).
- [28] P. Gaunt, Ferromagnetic domain wall pinning by a random array of inhomogeneities, *Philos. Mag.* **B 48**, 261 (1983).
- [29] W. Yan, Ph.D. thesis, University of Cambridge, UK, 2014. Available at <https://doi.org/10.17863/CAM.84753>.
- [30] M. J. Donahue and D. G. Porter, *OOMMF User's Guide*, Version 1.0 NISTIR 6376 (National Institute of Standards and Technology, Gaithersburg, MD, 1999).
- [31] K. M. Lebecki, M. J. Donahue, and M. W. Gutowski, Periodic boundary conditions for demagnetization interactions in micromagnetic simulations, *J. Phys. D: Appl. Phys.* **41**, 175005 (2008).
- [32] K. Ramstöck, W. Hartung, and A. Hubert, The phase diagram of domain walls in narrow magnetic strips, *Phys. Status Solidi A* **155**, 505 (1996).
- [33] T. Higuchi, T. Yajima, L. Fitting Kourkoutis, Y. Hikita, N. Nakagawa, D. A. Muller, and H. Y. Hwang,  $\text{Mn}_3\text{O}_4$  precipitates in laser-ablated manganite films, *Appl. Phys. Lett.* **95**, 043112 (2009).
- [34] P. Perna, C. Rodrigo, E. Jiménez, F. J. Teran, N. Mikuszeit, L. Méchin, J. Camarero, and R. Miranda, Tailoring magnetic anisotropy in epitaxial half metallic  $\text{La}_{0.7}\text{Sr}_{0.3}\text{MnO}_3$ , *J. Appl. Phys.* **110**, 013919 (2011).
- [35] R. A. Hyman, A. Zangwill, and M. D. Stiles, Magnetic reversal on vicinal surfaces, *Phys. Rev. B* **58**, 9276 (1998).
- [36] J. H. Van Vleck, On the anisotropy of cubic ferromagnetic crystals, *Phys. Rev.* **52**, 1178 (1937).
- [37] C. Zener, Classical theory of the temperature dependence of magnetic anisotropy energy, *Phys. Rev.* **96**, 1335 (1954).
- [38] J. Wang, H. Duan, X. Lin, C. Aguilar, A. Mosqueda, and G. Zhao, Temperature dependence of magnetic anisotropy constant in iron chalcogenide  $\text{Fe}_3\text{Se}_4$ : Excellent agreement with theories, *J. Appl. Phys.* **112**, 103905 (2012).
- [39] J. M. D. Coey, *Magnetism and Magnetic Materials* (Cambridge University Press, Cambridge, 2009).
- [40] U. Atxitia, D. Hinzke, O. Chubykalo-Fesenko, U. Nowak, H. Kachkachi, O. N. Mryasov, R. F. Evans, and R. W. Chantrell, Multiscale modelling of magnetic materials: Temperature dependence of the exchange stiffness, *Phys. Rev. B* **82**, 134440 (2010).